



# In situ patterning of nickel/sulfur-codoped laser-induced graphene electrode for selective electrocatalytic valorization of glycerol

Zhiliang Feng<sup>a</sup>, Zekun Geng<sup>a</sup>, Shuzhen Pan<sup>b</sup>, Yaru Yin<sup>a</sup>, Xinzhi Sun<sup>a</sup>, Xiaojuan Liu<sup>a</sup>, Lei Ge<sup>a,c,\*</sup>, Feng Li<sup>a,\*\*</sup>

<sup>a</sup> College of Chemistry and Pharmaceutical Sciences, Qingdao Agricultural University, Qingdao 266109, China

<sup>b</sup> Qingdao Petrochemical Advanced Technical School, Qingdao 266108, China

<sup>c</sup> Key Laboratory of Advanced Energy Materials Chemistry (Ministry of Education), Nankai University, Tianjin 300071, China

## ARTICLE INFO

### Keywords:

Glycerol  
Electrocatalytic oxidation  
Dihydroxyacetone  
Laser-induced graphene  
Heteroatom-doped

## ABSTRACT

The electrocatalytic valorization of glycerol is an emerging upcycling process for the biomass utilization. In this work, nickel/sulfur-codoped laser-induced graphene (LINiSG) on flexible polyimide film was fabricated and demonstrated as a self-supported and binder-free monolithic electrode for electrocatalytic glycerol oxidation reaction (EGOR) towards the selective generation of value-added three-carbon (C3) chemicals. The laser-induced in-situ and synchronous carbonization of polysulfone and Ni precursor was demonstrated to remarkably promote both the electrochemical surface area and Ni loading of LINiSG electrode. These synergistic merits are considered as the main origin for its enhanced EGOR activity and stability, showing much smaller Tafel slope and 2-fold enhanced current density, as compared to LINiG electrode without the co-carbonization of polysulfone. The influence of experimental parameters has been systematically investigated by the product analysis, achieving an average 94.7 % C3 selectivity and 76.1 % C3 Faradaic efficiency with a high selectivity of dihydroxyacetone (ca. 67.7 %) in near-neutral conditions, which is better than most of the reported EGOR electrodes operated in near-neutral conditions. This work demonstrated the viability of using flexible self-supported and binder-free LiG electrode with rational design and preparation approach for electrocatalytic valorization of biomass.

## 1. Introduction

In response to the global energy crisis and the carbon emissions related to the large consumption of fossil fuels and petroleum-derived feedstocks, the development and utilization of renewable biomass resources, one of the widely available but underutilized sources on earth, is encouraged as alternatives to fossil fuels and feedstocks for the carbon neutralization and green environment [1]. In this regard, the catalytical conversion of abundant and sustainable biomass resources or biomass-derived feedstocks into fine chemicals and green fuels has received increasing academic interest and plays a significant role in upcycling strategies of the “Waste-to-Treasure” process [2]. Among various biomass-derived feedstocks, glycerol (GLY), a massively produced unavoidable by-product originating of the rapidly growing biodiesel manufacture (≈100 kg GLY per one ton biodiesel), has been regarded as a low price (≈0.17 US\$/kg) and top ten biomass-derived molecules with vast availability [3,4]. Being in surplus supply with

low price, the oxidative valorization of GLY into fine chemicals is not only a promising solution to fully utilize GLY, but also brings high economic benefits [5]. As a three-carbon (C3) polyhydroxyl molecule, the three active hydroxyl groups of GLY allow the easy occurrence of GLY oxidation reaction (GOR), generating various value-added oxygen-functionalized organic products [3], such as dihydroxyacetone (DHA), glyceraldehyde (GLAD), lactic acid (LA), glyceric acid (GLA), tartronic acid (TA), and mesoxalic acid (MA), which can also be further oxidized into C1/C2 products coupled with the occurrence of oxidative C-C cleavage, such as glycolic Acid (GA), oxalic Acid (OA), and formic acid (FA). Among these valuable products of glycerol oxidation, DHA (≈US \$150 per kg) is particularly interesting with higher economic value than GLY, because it can be expansively used in the synthesis of cosmetics, food additives, pharmaceutical production, and so on [6]. As the smallest sugar molecule in nature, GLAD is an industrially important chemical, with wide commercial applications in the synthesis of polyesters, adhesives, antibiotics, and anticancer drugs [7]. GLA is also

\* Corresponding author at: College of Chemistry and Pharmaceutical Sciences, Qingdao Agricultural University, Qingdao 266109, China.

\*\* Corresponding author.

E-mail addresses: [lge@qau.edu.cn](mailto:lge@qau.edu.cn) (L. Ge), [lifeng@qau.edu.cn](mailto:lifeng@qau.edu.cn) (F. Li).

<https://doi.org/10.1016/j.apcatb.2024.124101>

Received 20 February 2024; Received in revised form 11 April 2024; Accepted 18 April 2024

Available online 21 April 2024

0926-3373/© 2024 Elsevier B.V. All rights reserved.

widely utilized as a personal care product in medicine and skincare treatment and as a base material for functional surfactants, e.g., rust removal and degreasing agent, and monomers for organic synthesis of oligoesters or polymers [8].

Owing to the utilization of clean and renewable electricity (solar, wind, and tidal), electrocatalytic refinery of GLY in water at ambient temperature and atmospheric pressure is a greener and more sustainable approach towards glycerol valorization into value-added chemicals in comparison with the traditional thermal catalytic one that usually relies on both unrenewable fossil fuels and environmental-unfriendly chemical oxidants [9]. Moreover, electrocatalytic GOR (EGOR) can be coupled with hydrogen evolution [10,11], CO<sub>2</sub> reduction [12] or nitrate reduction [13] to not only bypass the kinetically sluggish and energy-consuming anodic oxygen evolution reaction (OER) but also enable the efficient and selective simultaneous electro-synthesis of high value-added chemicals at both the anode and cathode with low energy consumption [14]. Besides the extensive research on noble metals [15–18], the oxides [19–22], sulfides [23], phosphides [24], or hydroxides [25,26] of several earth abundant transition metals like Ni, Cu, and Co as well as their composites [27–29] have been proven to provide more favorable and competitive catalytic performance in alcohol oxidation due to their low-prices, easy fabrication, excellent stability, and impressive selectivity, making earth abundant transition metal a promising alternative for noble metal-based electrocatalyst in GLY valorization. To enhance the electron transfer rate and chemical stability of transition metal-based electrocatalysts during alcohols electro-oxidation reaction, various carbon materials have been employed as highly conductive substrates to construct a heterogeneous interface with good dispersion of electrocatalysts [30–32]. In particular, heteroatom (nitrogen (N), sulfur (S)) doped 3D porous carbon materials can not only facilitate faster mass/electron transport, but also provide a 3D porous structure with large surface area and rapid mass transport, thus exposing more electrocatalytic active sites [33–35]. Although introducing heteroatom-doping carbon materials can boost the EGOR performance of transition metal-based electrocatalysts through providing more anchor sites for transition metal-based nanoparticles as well as improving the conductivity of the composites [30,36], the fabrication processes of these composite nanomaterials generally involved complicated procedures with high temperature/pressure [37–39]. Moreover, most of the developed electrodes have been exclusively dedicated on the pre-preparation of electrocatalysts, and thus the use of Nafion as polymer binder is highly required to immobilize the as-prepared electrocatalysts in powder form onto the surface of conductive current collectors for making electrodes, which would bring about manipulative complexity and cost issues [40,41]. Therefore, it is urgent to develop a more facile and greener method with good controllability and patternability for the large-scale preparation of self-supported and binder-free monolithic electrodes with abundant active sites in the three-dimensional porous heteroatom-doped carbon structure with rapid mass/electron transport and high EGOR performance.

Recently, the emerging carbon material of laser-induced graphene (LIG) fabricated under ambient conditions has attracted extensive attention [42,43], not only due to its fast and programmable laser-scanning process in a non-contact, mask-free, and solid-phase-transition mode without the usage of any catalyst. but also because of its good compatibility with many substrates ranging from polymers to biomass materials such as paper, wood, and leaf [44]. The fast and facile synthesis of LIG is usually realized by the photothermal effect of an accurately controlled CO<sub>2</sub>-laser beam scanned on the surface of precursors (such as polyimide film) at room temperature in the air, instantaneously generating a high localized temperature (>2500 °C) at the desired position, which triggers the fast carbonization of the irradiated precursors to form LIG with well-defined 3D macroporous network architecture and desired patterns [45,46]. Moreover, precursors that contain heteroatoms (such as N, S, B, F) in their own molecular groups and/or metal ions doped precursors can be employed to

fabricate heteroatom-doped LIG with additional atomic/structural defects and/or diverse functional materials, showing enhanced electrical conductivity and electrochemical property due to their synergistic effect [45]. The aforementioned unique properties make the LIG technique promising for versatile electrode fabrications [47] with simplified patterning and scalable manufacturing towards various applications including (photo)electrochemical sensors [48], electro-energy storage [49], and electrocatalysis [50]. In the field of electrocatalysis, LIG-based electrodes have exhibited attractive properties in a variety of electrocatalytic reactions [51–53]. However, the use of LIG-induced electrocatalysts for EGOR has not received sufficient attention so far to the best of our knowledge. Tse's group was the only one to report a laser-assisted nanomaterial preparation method for direct solid phase synthesis of bimetallic-LIG hybrid electrocatalysts from metal nanolayer modified PI films and produced a new binder-free electrode on indium tin oxide (ITO) conductive glass for efficient and selective EGOR [7]. However, both the tedious pretreatment procedures to incorporate the metal nanolayer on PI surface and the time-consuming post-heat treatment procedures to enhance the crystallinity of electrocatalysts as well as the use of expensive ITO current collectors diminish its accessibility for practical electrocatalytic application. Therefore, the LIG technology offers an opportunity to construct a self-supported and binder-free monolithic electrode with non-noble metal EGOR electrocatalysts with simplified operation and decreased cost, even though it is still in its infancy.

Herein, an improved direct-laser-writing method was demonstrated for facile and straightforward preparation of binder-free and self-standing EGOR electrode, which was fabricated by one-step CO<sub>2</sub> laser-scanning on the Ni<sup>3+</sup>-polysulfone (Ni<sup>3+</sup>-PSU)-loaded flexible LIG/PI sheet in solid phase at ambient temperature and pressure. As a typical electrocatalyst, Ni-based nanomaterials have been reported to demonstrate comparatively faster reaction kinetics for the EGOR, with inherent selective dehydrogenation properties [6]. The exposure of Ni<sup>3+</sup>-PSU film to CO<sub>2</sub> laser-scanning leads to the in situ, fast, and synchronous formation of S-doped LIG and Ni-based nanoparticles homogeneously embedded in S-doped LIG as electrocatalysts for EGOR with narrow particle size distribution. The 3D macroporous structural properties of LIG are intrinsically inherited by the laser-induced Ni/S-codoped LIG hybrids, denoted as LINiSG, with high surface area and stable architecture. Unlike the traditional drop-casting method, the flexible PI film supported LINiSG hybrids could be directly used as binder-free and self-standing monolithic electrode for EGOR, based on which a selective electrocatalytic upcycling process to convert GLY to value-added C3 products, including DHA and GLAD, in a near-neutral electrolyte solution (pH = 9) was demonstrated with good activity and reasonable stability. The electrocatalytic performances of LINiSG electrode for EGOR such as production rates, product distribution, and Faradaic efficiency (FE) for EGOR are systematically investigated by simply modulating the electrode compositions and operation conditions, such as the applied potential, temperature, laser power, pH values, and the loading of Ni mass. As the dominant product, a high yield of DHA (average 67.7 % selectivity and 51.6 % FE) with an average production rate of 3.3 μM cm<sup>-2</sup> min<sup>-1</sup> can be obtained via the selective secondary hydroxyl oxidation of GLY on LINiSG electrode, exceeding most reported electrodes operated in near-neutral electrolytes. The proposed convenient method will contribute to the green and facile fabrication of self-supported and binder-free monolithic electrode with high-performance synergistic effects for EGOR, which may be of great use for future electrochemical valorization of various biomass-derived feedstocks.

## 2. Experimental section

### 2.1. Reagents and materials

Nickel acetylacetonate (Aladdin, 95 %), glycerol (GLY, Macklin,

≥99.5 %), DL-glyceraldehyde (GLAD, Macklin, 90 %), glyceric acid (GLA, Macklin, 20 % in water, 2 M), 1, 3-dihydroxyacetone (DHA, Macklin, 99 %), tartronic acid (TA, Macklin, 98 %), DL-lactic acid (LA, Macklin, 85–90 %), hydroxypyruvic acid (HPA, MCE, ≥95 %), glycolic acid (GA, Macklin, 98 %), Glyoxylic acid monohydrate (GLOA, Macklin, 98 %), oxalic acid (OA, Aladdin, 99.999 %), acetic acid (AA, Maklin, 99.9 %), formic acid (FA, Macklin, ≥99 %), 1-methyl-2-pyrrolidinone (NMP, Aladdin, >95 %), dimethyl sulfoxide (DMSO, Macklin, >99.8 %), potassium sulfate (Sinopharm Chemical Reagent Co., Ltd., ≥99 %), boric acid (H<sub>3</sub>BO<sub>3</sub>, Sinopharm Chemical Reagent Co., Ltd., ≥99.5 %) were used without further purification. Polysulfone (PSU) polymer powders were obtained from Trump Chemical Corporation. Kapton polyimide (PI) sheet (500HN, thickness: 125 μm) were purchased from DuPont. Prior to use, the PI sheets were ultrasonically cleaned in acetone, ethanol, and water, respectively, for 30 min each, followed by washing copiously with ultrapure water and blown dry under a stream of N<sub>2</sub> gas. The ultrapure water (resistivity of 18.2 MΩ cm at 25 °C) was provided by a Milli-Q water purification system (Millipore Corp., Bedford, MA, USA). A 0.75 M sodium borate buffer (Na<sub>3</sub>BO<sub>3</sub>) was prepared by adjusting the pH of a 0.75 M H<sub>3</sub>BO<sub>3</sub> solution to 9.0 with NaOH powder and used as the electrolyte.

## 2.2. Fabrication of LINiSG electrode

A commercial Epilog Laser engraving machine was utilized as a printer to perform the laser patterning, which equipped with a built-in 10.6 μm CO<sub>2</sub> laser tube. Laser spot was focused on the top surface of PI film. Firstly, a designed pattern (1 × 1 cm<sup>2</sup> square) was scanned onto the PI film surface, with an image density of 1200 pulses per inch (PPI), 8 % of full laser power, and 10 % of full scanning speed, to straightforwardly carbonize PI film surface into LIG with the desired pattern under ambient conditions. Then, 385.4 microgram of Ni(acac)<sub>2</sub> and 0.5 g of PSU polymer was successively dissolved in 5 mL of DMSO/DMF mixed solvent (v/v 1: 4) with continuous stirring at room temperature. The resulting mixture was continuously stirred to form a homogeneous Ni ion-containing PSU solution (Ni<sup>2+</sup>-PSU) and then dropped into the freshly prepared LIG patterns, followed by 5 min incubation under ambient conditions. After vacuum drying at 80 °C, the Ni<sup>2+</sup>-PSU soaked LIG was lased again atop a new 1 × 2 cm<sup>2</sup> rectangle pattern under the same conditions, where the 1 × 1 cm<sup>2</sup> Ni<sup>2+</sup>-PSU square was directly transformed into LINiSG hybrid film connected with a freshly generated 1 × 1 cm<sup>2</sup> LIG pattern as the contact pad, which was then separated to the LINiSG area by sealing an epoxy passivation line between them to protect the contact pad from electrolyte and maintain a constant working area on the electrode. Finally, conductive colloidal silver ink was painted on the LIG contact pad (1 × 1 cm<sup>2</sup>) to improve the conductivity. Five LINiSG hybrid films were then connected with Cu tape and used as an integrated working electrode (Fig. S1). For comparison, the LiSG, LINiG, and LIG electrode were also prepared under the same conditions without the addition of Ni(acac)<sub>2</sub> and/or PSU before the second laser scanning.

## 2.3. Characterization

X-ray diffraction (XRD) patterns were collected with a Bruker D8 diffractometer (Germany) using Cu Kα as the radiation source over the 2θ scan range of 20–70°. X-ray photoelectron spectroscopy (XPS) measurements were performed on a ESCALAB 250Xi instrument (Thermo Fisher, Waltham, MA, Al Kα radiation). Scanning electron microscopy (SEM) images were recorded using a FEI QUANTA Q400 electron microscopy operating at an accelerating voltage of 20 kV. Transmission electron microscopy (TEM) images, high-resolution transmission electron microscopy (HRTEM) images were obtained on a FEI microscope (Tecnai G2 F30) with a 300 kV accelerating voltage. Raman spectra were measured by a DXRxi Raman spectrometer (Thermo Scientific) with an excitation wavelength of 532 nm. Metal contents in

electrodes were determined by inductively coupled plasma optical emission spectroscopy (ICP-OES, PerkinElmer 8000 DV, USA). For ICP-OES measurements, all the samples were collected from the PI film via thorough ultrasonication in ethanol and then dried at 60 °C, followed by the digestion in 2.0 mL HCl: HNO<sub>3</sub> (v/v 3:1) solution for two days. Then, the obtained solution was diluted 100 times and filtered with a 0.22 μm syringe filter. Electrochemical impedance spectroscopy (EIS) spectra were measured at an applied potential of 1.62 V<sub>RHE</sub> in 0.75 M borate buffer (pH = 9) with 100 mM GLY over a range of 10<sup>6</sup> to 10<sup>-2</sup> Hz. Static water contact angles were measured at room temperature by means of a standard contact-angle measuring instrument (KRÜSS DSA25) employing drops of pure water.

## 2.4. Electrochemical measurements and product quantification

All electrochemical measurements for GLY oxidation were performed using a typical three-electrode configuration in Ar-saturated 0.75 M sodium tetraborate electrolyte with/without 100 mM GLY at ambient conditions, unless otherwise specified, on an electrochemical workstation (CHI 660E, CH Instruments, Inc.) and the results of which were displayed without *iR*-correction in this work. All electrode potentials measured against Ag/AgCl were calibrated to the reversible hydrogen electrode (RHE) scale. Before each electrochemical measurement, the working electrode was activated by cyclic voltammetry (CV) method in 1.0 M KOH in a potential range of 0.9–2.1 V<sub>RHE</sub> for 50 cycles at a scan rate of 50 mV s<sup>-1</sup>. The electrochemical tests were performed in an undivided glass beaker, using self-supporting integrated electrode (1 cm<sup>2</sup> × 5 total geometric area) as working electrode, Ag/AgCl electrode (with saturated KCl solution) as reference electrode, and Pt foil as counter electrode. Linear sweep voltammetry (LSV) curves of these electrodes were acquired from 0.63 V to 1.83 V<sub>RHE</sub> at a scan rate of 2 mV s<sup>-1</sup>.

The electrocatalytic oxidation of GLY was carried out in a self-made divided H-type reactor separated by Fumasep FAB-PK-130 anion exchange membrane. Chronoamperometry method was adopted to apply a constant potential of 1.62 V<sub>RHE</sub> and record the current density with Ag/AgCl and Pt sheets as reference and counter electrode, respectively. The cathode electrolyte was 45 mL of 0.75 M borate buffer (pH = 9) and the anodic chamber for GLY oxidation contains 45 mL of 0.75 M borate buffer (pH = 9) + 100 mM GLY, which was stirred continuously at 500 rotations min<sup>-1</sup>. After passing certain charges, 1.0 mL of the electrolyte solution were taken out from the anodic chamber and immediately acidified for subsequent analysis of EGOR products. The above liquid products were filtered with a 0.22 μm syringe filter and then analyzed by high performance liquid chromatography (HPLC; Thermo Scientific UltiMate 3000 HPLC) equipped with Hi-Plex H column (300 × 7.7 mm) with a Hi-Plex H guard column, using 5 mM aqueous H<sub>2</sub>SO<sub>4</sub> as mobile phase (0.6 mL min<sup>-1</sup> at 65 °C) and detected by UV detector with multiple wavelengths (194 nm, 210 nm, and 270 nm). All products were measured by the three wavelengths at the same time to give the best product quantification with an external calibration method.

The Faradic efficiency of the desired EGOR product were calculated using the following formula.

$$FE_{\text{product}} = (n_e \times n_{\text{product}} \times F)/Q \times 100 \% \quad (2)$$

where  $n_e$  is the number of electrons required to form the desired product per molecule [6], which is calculated according to the balanced half-reactions shown in [Supplementary Material](#);  $n_{\text{product}}$  is the mole of the desired product,  $F$  is Faraday constant (96485 C mol<sup>-1</sup>);  $Q$  is the total quantity of electric charge pass through the working electrode during EGOR.

The relative selectivity of the desired product and corresponding production rate was calculated using the following equations:

$$\text{Selectivity}_{\text{product}} = n_{\text{product}}/n_{\text{total}} \times 100 \%$$

$$\text{Production rate} = n_{\text{product}} / (t \times m_{\text{catalysts}} \times A)$$

Where  $n_{\text{product}}$  is the mole of the desired product,  $n_{\text{total}}$  is the micro-mole of all products,  $t$  (min) is the reaction time, and  $A(\text{cm}^{-2})$  is the total geometry area of electrode.

### 3. Results and discussion

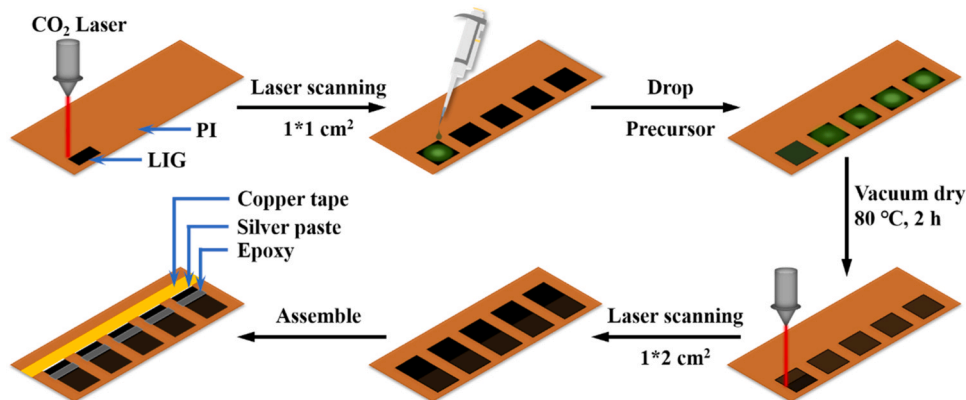
The fabrication process of LINiSG electrode is schematically illustrated in Scheme 1. Firstly, LIG were patterned on the PI sheet by CO<sub>2</sub> laser scanning in ambient air as a 1×1 cm<sup>2</sup> squares. Upon exposure to CO<sub>2</sub> laser, the brown PI film was turned into black LIG patterns where the laser scanned, which was employed as both the conductive matrix and precursor absorption layer due to its 3D macroporous architectures. Then, the polysulfone (PSU) precursor solution containing nickel acetylacetonate was uniformly added into the 3D structure of the existing square LIG patterns on PI sheet, followed by a drying process. Here, PSU is selected as the role of both carbon and sulfur dopant sources due to its easy graphitization, high charring performance, and good stability in air. Benefiting from the simple patterning of the LIG, various customized shapes can be directly patterned on the substrate surface via a facile computer-controlled design. Thus, the fabrication of 3D macroporous LINiSG hybrid and patterning of LIG contact pad were facilely achieved in one step by direct-laser-writing on the precursor-loaded flexible LIG/PI sheet with a precisely controlled rectangular pattern (1 × 2 cm<sup>2</sup>), without the requirements of any protective gas atmosphere, harmful conditions (ca. high temperature/pressure), toxic reagents (ca. catalyst/oxidant/template), and post thermal annealing. During the laser-patterning, Ni ions were in situ converted into Ni<sup>0</sup> or oxide nanoparticles, which are uniformly anchored into the LIG and can act as electrocatalytic active sites for EGOR. Meanwhile, sulfur atoms in PSU molecules can be successfully doped into LIG, yielding Ni/S-codoped LIG with more electrocatalytic activities for EGOR through their synergistic effects. Through the above ingenious design, five LINiSG hybrid films with conductive LIG current collector and Ni/S-codoped LIG electrocatalysts were interconnected and integrated on the flexible PI film as a self-standing and binder-free electrocatalytic EGOR electrode (Fig. S1). For comparison, another three LIG-based electrodes without the addition of Ni and/or PSU precursor were also prepared under the same conditions, denoted as LIG, LINiG, and LISG, to verify the superiority of LINiSG hybrid electrode.

The formation of LIG in all electrodes was first confirmed by Raman spectra via the appearance of three typical D, G, and two-dimensional (2D) bands of graphene centered at around 1340, 1573, and 2675 cm<sup>-1</sup> wavenumbers (Fig. 1A), which could be indexed to disordered or defective sp<sup>3</sup> hybridized carbon in the graphene lattices, in-plane vibration of ordered sp<sup>2</sup>-type graphitic carbon, and second-order zone-boundary phonons, respectively, revealing the successful graphitization of the PI and/or PSU in these electrodes. The I<sub>D</sub>/I<sub>G</sub> ratios for all electrodes are around 0.93–1.04 (Fig. 1B), suggesting the high defect

percentage or bent graphenic structure in LIG skeletons, which is, however, conducive to interface electron transfer and electrochemical performance of LIG. Compared with others, the I<sub>D</sub>/I<sub>G</sub> ratio of LINiG electrode increases obviously, indicating that the mere addition of nickel acetylacetonate tends to destroy the ordered sp<sup>2</sup>-type graphitic structure of LIG probably due to the in-situ formation of Ni-based electrocatalysts embedded onto LIG domains. Moreover, the recovered I<sub>D</sub>/I<sub>G</sub> ratios of LISG and LINiSG electrodes imply that the addition of PSU favors the simultaneous formation of Ni-based electrocatalysts and S-doped LIG, which is possibly resulted from the enhanced laser energy absorption by the PSU precursors. Furthermore, the I<sub>2D</sub>/I<sub>G</sub> ratios of LINiG (0.48), LISG (0.47), and LINiSG (0.53) are close to that of LIG (0.56) (Fig. 1B), indicating that all samples are composed of 3D multi-layered graphene structures with similar graphitization degrees, and demonstrating that the laser-induced hybrid electrodes well preserve the characteristics of LIG in the presence of Ni and/or PSU.

The presence of LIG and Ni-based electrocatalyst in these as-prepared electrodes were further characterized by XRD. As displayed in Fig. 1C, the XRD patterns of the four samples all show two distinct diffraction peaks located at 2θ = ~25.9° and 42.9°, corresponding to the (002) and (100) inter-plane of LIG, respectively. Apart from the LIG features, the LINiG electrode has distinguished peaks at 2θ = 37.3°, 43.2°, 44.3°, 51.6°, and 62.9°, which is known to originate from (111) and (200) characteristic planes of metallic Ni species (PDF#89-7128) as well as (111), (200), and (220) in-plane reflections of NiO (PDF#47-1049), respectively, demonstrating the successful conversion of nickel acetylacetonate into metallic Ni<sup>0</sup> and oxide under laser scanning. The XRD pattern of LISG shows similar diffraction peaks with that of LIG electrode, indicating that the laser-scribing of PSU has no influence on the crystal structure of LIG. Moreover, LINiSG electrode only shows two additional characteristic peaks of metallic Ni<sup>0</sup> (PDF#89-7128) at 2θ = 44.3° and 51.6°, proving the formation of metallic Ni<sup>0</sup> nanocrystals. However, no obvious XRD peaks of NiO were detected in LINiSG electrode.

Therefore, the chemical states and composition of Ni-based electrocatalysts was further clarify by XPS. As indicated in Fig. 1D and Fig. S2A, the high-resolution Ni 2p<sub>3/2</sub> peaks of the LINiSG and LINiG electrodes were deconvoluted into two valence states of Ni<sup>0</sup> and Ni<sup>2+</sup> [54], indicating that partial Ni<sup>2+</sup> has been reduced to Ni<sup>0</sup> due to the carbothermic reaction upon laser-scribing that forms the metallic Ni<sup>0</sup> nanoparticles. The O 1s core level spectra of the LINiSG (Fig. 1E) and LINiG (Fig. S2B) electrode exhibits two distinct peaks: the peak centered at about 532 eV associates with the oxygen-containing groups such as C-O, C=O, and S-O bonds from S-doping LIG [55] as well as the absorbed oxygen pieces; and a shoulder feature at a lower binding energy of about 530 eV, which originates from M-O bonds within a regular oxide crystal, here, the lattice oxygen of the NiO phase, proving the existence of NiO in both LINiG and LINiSG electrode [55]. In addition to a prominent peak



**Scheme 1.** Schematic illustration for the fabrication process of LINiSG electrode containing five interconnected LINiSG hybrid films.



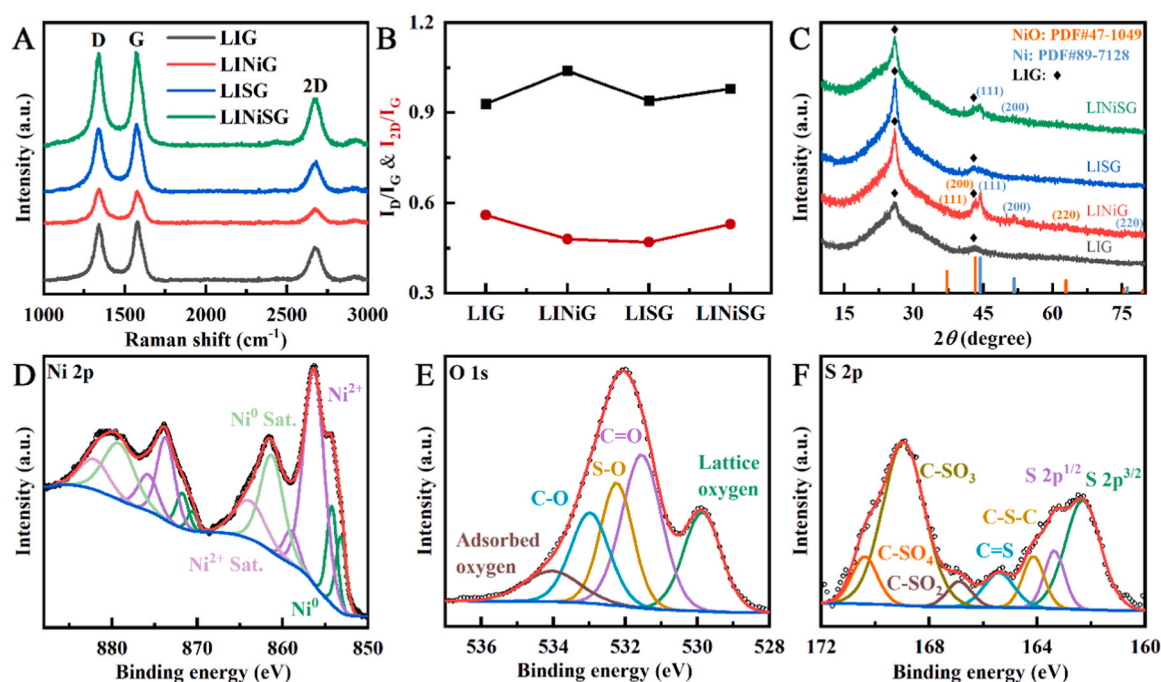


**Fig. 1.** A) Raman spectra and B) summary of  $I_D/I_G$  (black squares) and  $I_{2D}/I_G$  (red dots) ratios of different electrodes; (C) XRD patterns; High-resolution D) Ni 2p, E) O 1 s, and F) S 2p XPS of LINiSG electrode.

centered at binding energy of about 169 eV for oxygen-containing sulfur groups ( $C-SO_x$ ,  $x = 2, 3, 4$ , respectively) [48] in both LINiSG (Fig. 1F) and LISG (Fig. S3C) electrode, the S 2p core level region of the LINiSG electrode exhibits four new obvious XPS peaks with the remarkable decline of oxygen-containing sulfur groups. The emerged S 2p peak at around 165.4 and 164.2 eV can be ascribed to the  $C=S$  and  $C-S-C$  groups [48], respectively, indicating that the presence of the nickel acetylacetonate contributes to the formation of S-doping LIG. Meanwhile, the fitting peaks at 163.4 and 162.3 eV can be well assigned to  $S 2p_{1/2}$  and  $S 2p_{3/2}$ , corresponding to the generation of  $S^{2-}$  state [48], which are indicative of the coexistence of NiS in the LINiSG electrode.

The SEM images in Fig. 2 disclose the 3D holey foam-like structure of these electrodes and are dependent on the fabrication precursors. The surface morphology of LIG electrode has the appearance of highly porous LIG patterns (Fig. 2A) arranged in a parallel orientation to the scanning direction of laser beam. The fabricated LINiG electrode after the second laser-scribing almost inherits the surface morphology of the original LIG electrode (Fig. 2B). However, fiber-type LIG microstructures (LIG grasses) are observed in LISG electrode (Fig. 2C). With the further addition of Ni precursor, the density of LIG grasses increases in LINiSG electrode as shown in Fig. 2D, which is conducive to a boost of the accessible surface area between the electrolyte and the electrode interface. Higher magnified SEM images in Fig. S4 clearly show that all electrode surfaces exhibited typical 3D macroporous cross-network architecture composed of multi-layered interconnected graphene flakes and/or fibers due to the rapid generation and liberation of gases during laser-induced local photothermal reaction. The transient heating and cooling of laser-scribing could also effectively inhibit the aggregation of both graphene sheets/fibers and electrocatalysts in LIG structure, which is also corroborated by the homogeneous distribution of C, S, O, and Ni in the corresponding elemental mapping results (Fig. S5), providing multidimensional channels for electron and mass transport. Moreover, the intact 3D microstructures with the exposure of abundant edge-plane defect sites, consistent with the high  $I_D/I_G$  ratios observed by Raman spectra, is anticipated to enhance electrocatalytic activity. The TEM images in Fig. 2E also demonstrates the homogeneous distribution of electrocatalysts nanoparticles (about 10–50 nm) anchored on the

surface of multilayered LIG sheets. In the high-resolution TEM images, the presence and identity of the NiO (Fig. 2F) and Ni<sup>0</sup> (Fig. S6) electrocatalysts nanoparticles is confirmed by the interplanar distance of ca. 0.241 nm and 0.206 nm, respectively, corresponding to the (111) crystal plane of NiO and Ni<sup>0</sup> in line with XRD analysis.

The electrocatalytic GOR performance of these laser-induced electrodes were then evaluated via linear sweep voltammetry (LSV) in a customized H-shaped cell. As well-known, basic electrolyte solution with high pH will lead to the deep oxidation of GLY to formate [25,27], thus a near-neutral solution of 0.75 M borate buffer (pH = 9) was selected here as supporting electrolyte. The current density was normalized by the total geometric area ( $1 \text{ cm}^2 \times 5$ ) of electrodes to show the geometric current densities. In the absence of GLY (Fig. 3A), LIG and LISG electrodes show no obvious oxidation peak in 0.75 M borate buffer solution except a weak current increase from the emerging OER at high potentials. In contrast, LINiG and LINiSG electrodes exhibit a well-defined oxidation peaks centered at  $\sim 1.61 \text{ V}_{\text{RHE}}$ , corresponding to the electrochemical transformation from  $Ni^{2+}$  to  $Ni^{3+}$  in laser-induced Ni electrocatalysts, in which the formed  $Ni^{3+}$  has been considered as the real active sites toward the anodic oxidation of water and/or biomass [6]. In the presence of 100 mM GLY, LIG and LISG electrodes display a slightly decreased current density even at high potentials (Fig. 3A) maybe due to the passivation of electrode surface by GLY molecules, indicating low EGOR activity. Whereas LINiG and LINiSG electrodes show a significant increase in current density at the same potentials along with the disappearance of  $Ni^{2+}/Ni^{3+}$  peak, suggesting the preferred EGOR over OER on LINiG and LINiSG electrodes, which are contributed by the Ni oxidation in the laser-induced Ni electrocatalysts. Meanwhile, compared with the LINiG electrode, the Tafel slope of the LINiSG electrode (Fig. 3B) is smaller with an obviously reduced potential (Fig. 3C), which suggests a more rapid electrocatalytic reaction kinetic profile for the EGOR on the LINiSG electrode, in consistent with the LSV results, implying that the co-carbonization of PSU is conducive to enhance the EGOR performance. Moreover, the Nyquist plots of these electrodes shown in Fig. S7 presents two semi-circles at  $1.62 \text{ V}_{\text{RHE}}$  in 0.75 M borate buffer (pH = 9) with 100 mM GLY, corresponding to passivated film impedance at the

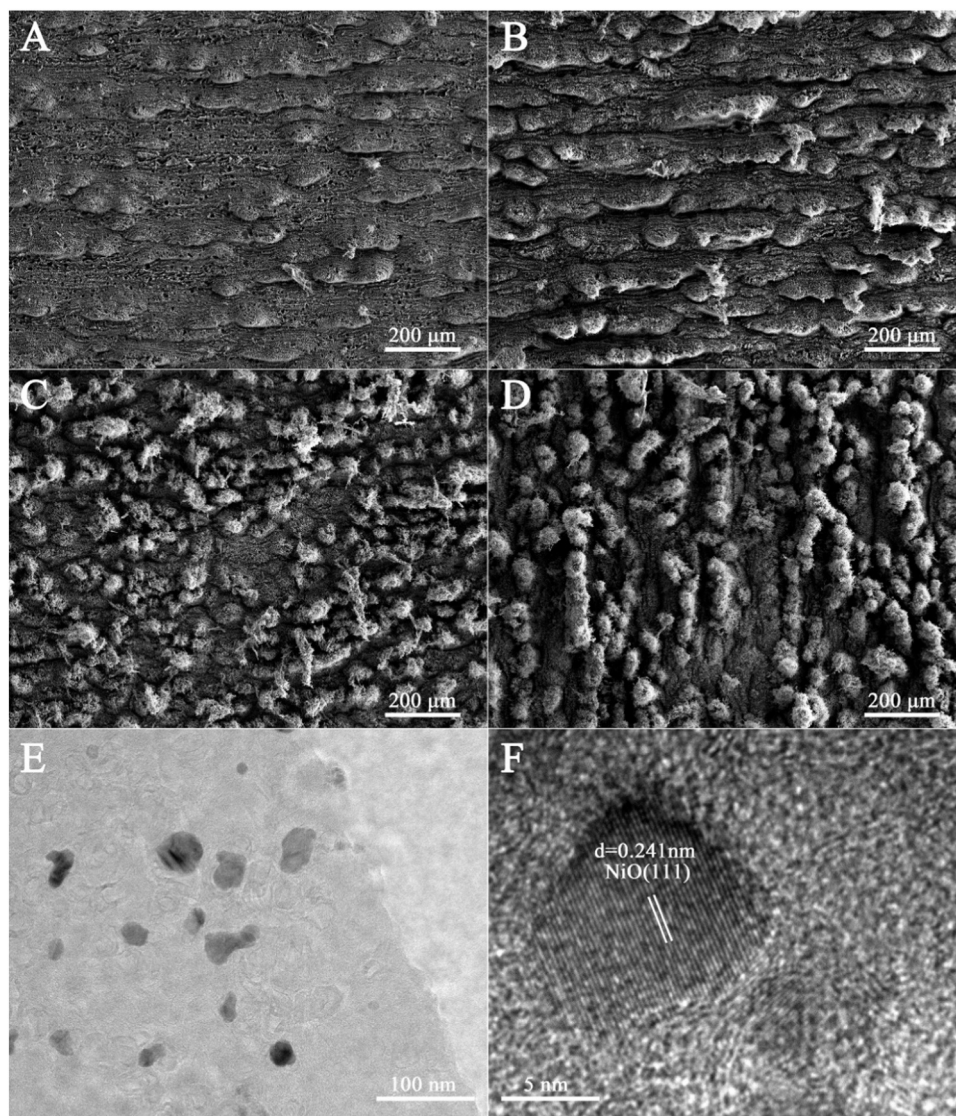


**Fig. 2.** Surface morphology of (A) LIG, (B) LINiG, (C) LISG, and (D) LINiSG electrodes; (E) TEM and (F) HRTEM images of the LINiSG electrode.

high-frequency region and charge transfer resistance at the low-frequency zone [50], respectively. It can be seen that the radius of both semi-circles over LINiSG electrode are the lowest under the same conditions, suggesting that the synchronous carbonization of polysulfone and Ni precursor can not only reduce the passivated film impedance but also facilitate charge transfer, thereby promoting EGOR performance from the perspective of kinetic.

Considering the different surface morphologies of the four electrodes, electrochemical surface area (ECSA) was first estimated by the double-layer capacitance ( $C_{dl}$ ) (Fig. S8), which was calculated via cyclic voltammogram (CV) measurements in the non-Faradic region with different scan rates and is expected to be linearly proportional to the ECSA. Among these electrodes, LINiSG electrode shows the largest  $C_{dl}$  value ( $3.62 \text{ mF cm}^{-2}$ ), while the  $C_{dl}$  values of LINiG, LISG, and LIG are 2.09, 1.95, and  $0.76 \text{ mF cm}^{-2}$  (Fig. 3D), respectively. Clearly, the  $C_{dl}$  value of LINiSG electrode is about 1.73 times than that of LINiG electrode, suggesting that the co-carbonization of PSU can markedly enlarge the ECSA associated with more exposed active sites. By comparing the ECSA-normalized current density (Fig. 3E), LINiSG electrode merely showing 1.2-fold higher than that of LINiG electrode, not correlated with the enhanced ECSA (ca. 1.73-fold) and geometric activities (ca. 2.0-fold at the same potentials, Fig. 3A), implying that the superior intrinsic EGOR activity of LINiSG is partially resulted from the increased ECSA of

LINiSG electrode. To further investigate the origin of the promoted electrocatalytic GOR activity observed for LINiSG electrode, the contribution of Ni mass toward electrocatalytic GOR activity was then evaluated. The Ni content analyzed by ICP-OES was utilized to calculate the mass activity of LINiSG and LINiG electrodes. As displayed in Fig. 3F, insert, the co-carbonization of PSU and nickel acetylacetonate exhibits a 3.0-fold higher Ni mass relative to the LINiG electrode, which should give LINiSG electrode a relatively abundant electrocatalytic active sites. However, after normalizing by Ni mass, LINiSG electrode exhibits a lower mass activity (Fig. 3F) compared with LINiG electrode, indicating the existence of many inaccessible active sites in the bottom layer of LINiSG electrode. Therefore, the contribution from the increased accessible Ni mass can not be fully ruled out. In short, it can be speculated that the enhanced intrinsic EGOR activity of LINiSG electrode might be related to the synergistic effect between the promoted ECSA, Ni mass, and the forming of S-doped LIG and even NiS electrocatalysts via co-carbonization of PSU.

To further validate the EGOR effectiveness on different electrodes, the liquid products of EGOR in the anode electrolyte were collected after a potentiostatic electrolysis at a potential of  $1.62 \text{ V}_{\text{RHE}}$  and were evaluated by high-performance liquid chromatography (HPLC) with calibration curves shown in Fig. S9. As a result of passing 36 C charges, barely no product was detected from the electrolyte solution of LIG and



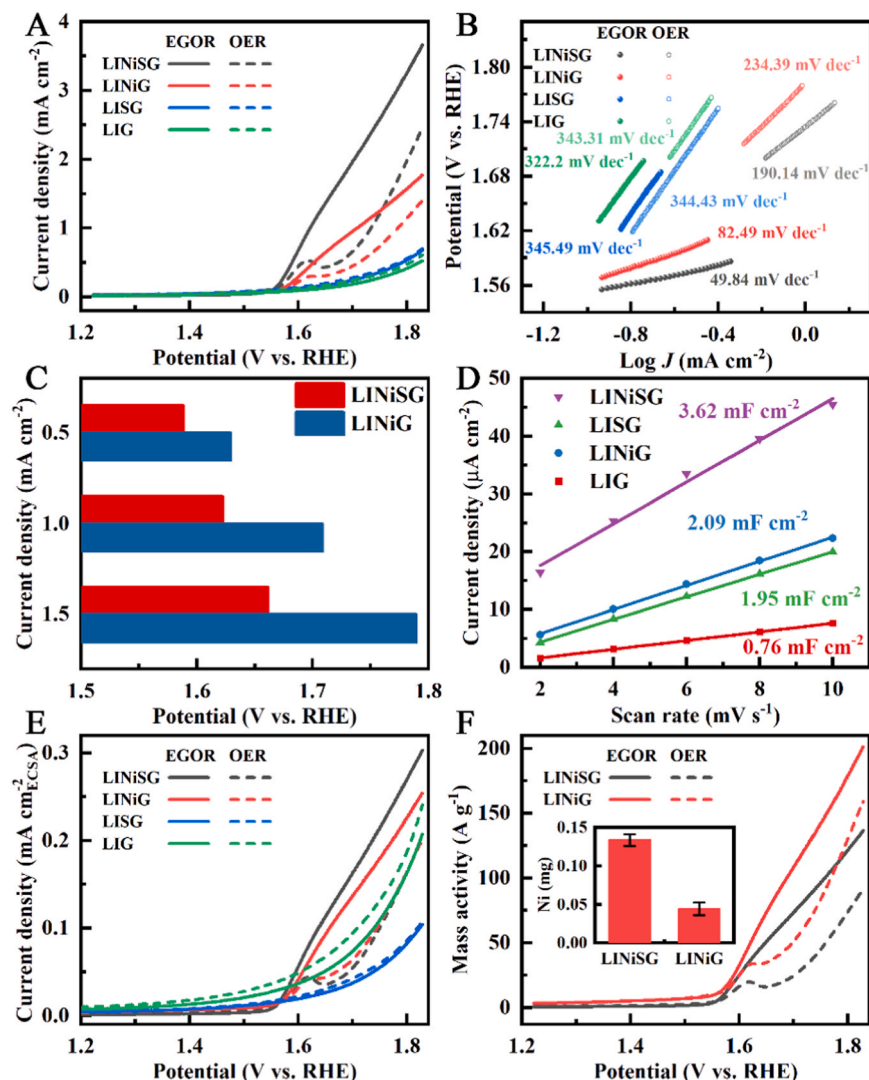


**Fig. 3.** (A) LSV curves and corresponding (B) Tafel slopes of LIG, LINiG, LISG, and LINiSG electrodes recorded in 0.75 M borate buffer without and with 100 mM GLY; (C) Required anodic potentials to drive certain geometric current densities; (D) The capacitive currents measured at 1.439 V<sub>RHE</sub> plotted as a function of scan rate; The same LSV curves in (A) after normalizing by (E) C<sub>dl</sub> and (F) Ni-mass; Insert is the Ni mass loadings of LINiG and LINiSG electrode.

LISG electrodes (Fig. 4A-C), while LINiG and LINiSG electrodes could produce three C3 chemicals (DHA, GLAD, and GLA) as the main product under the same conditions, emphasizing their superior EGOR performance. Along with C3 chemicals, GA (C2), and FA (C1) were also identified (Fig. 4A-C) in a limited amount as the subsequent oxidation products of C3 chemicals with C-C bond cleavage. Interestingly, the most valuable DHA is the dominant product on both LINiG and LINiSG electrode with an impressive selectivity throughout the whole electrolysis process, as presented in Fig. S10. Along with DHA, LINiSG electrode also yielded ~30 % GLYD and ~3 % GLA (Fig. 4D), making the C3 selectivity (S<sub>C3</sub>) and Faradaic efficiency (FE<sub>C3</sub>) substantially higher than that of LINiG electrode. The generation of C1 and C2 products on LINiSG electrode are greatly suppressed to a selectivity about 2 %, and the corresponding FE<sub>C1+C2</sub> was only 2.3 %. In contrast, the S<sub>C1+C2</sub> over the LINiG electrode is 14 % with a FE<sub>C1+C2</sub> as high as 10.8 %, which are indicative of a lower tendency for C-C bond cleavage on LINiSG electrode, verifying the critical role of PSU co-carbonization for EGOR. Moreover, the production rate of both C3 (3.4 μM cm<sup>-2</sup> min<sup>-1</sup>) and DHA (2.3 μM cm<sup>-2</sup> min<sup>-1</sup>) on LINiSG electrode exhibits more than 2-fold improvement compared with that of LINiG electrode (Fig. 4E), indicating the faster EGOR kinetics of LINiSG electrode, which is consistent with the results observed in LSV measurement (Fig. 3B). The high total

FE (FE<sub>total</sub>) of ca. 81 % towards all organic products discloses a low level of other redox processes on LINiSG electrode, such as OER. The efficient conversion of GLY into the valuable C3 products on the LINiSG electrode was demanded for later studies, especially the most valuable DHA.

The product distribution of LINiSG electrode at different potentials (1.57, 1.62, and 1.67 V<sub>RHE</sub>) were then investigated via collecting the anode electrolytes when the accumulated passed charges reached 3, 9, 18, 27, and 36 C, respectively. The resultant chronoamperometric curves with the total passed charges of 36 C were displayed in Fig. 4 F, in which the increasing trend of current density with the increase of applied potential is obvious, leading to a remarkably elevated production rate (Fig. 4G). The oxidation current shows a sharp decrease at the beginning due to the rapid decay of capacitive current followed by a slow decline over longer electrolysis time, as typically observed in electrocatalytic EGOR in weak-basic electrolyte solution [56], which can be attributed to the catalyst deactivation induced by the accumulation of chemisorbed intermediate species or caused by the leaching of the electrocatalyst as well as the decrease in the electrolyte pH. In all cases, the elongation of electrolysis time shows no significant influence on the product distribution (Fig. S11), indicating good stability of LINiSG electrode. Fig. 4H presented the typical potential-dependent product distribution profiles from EGOR over LINiSG electrode after passing

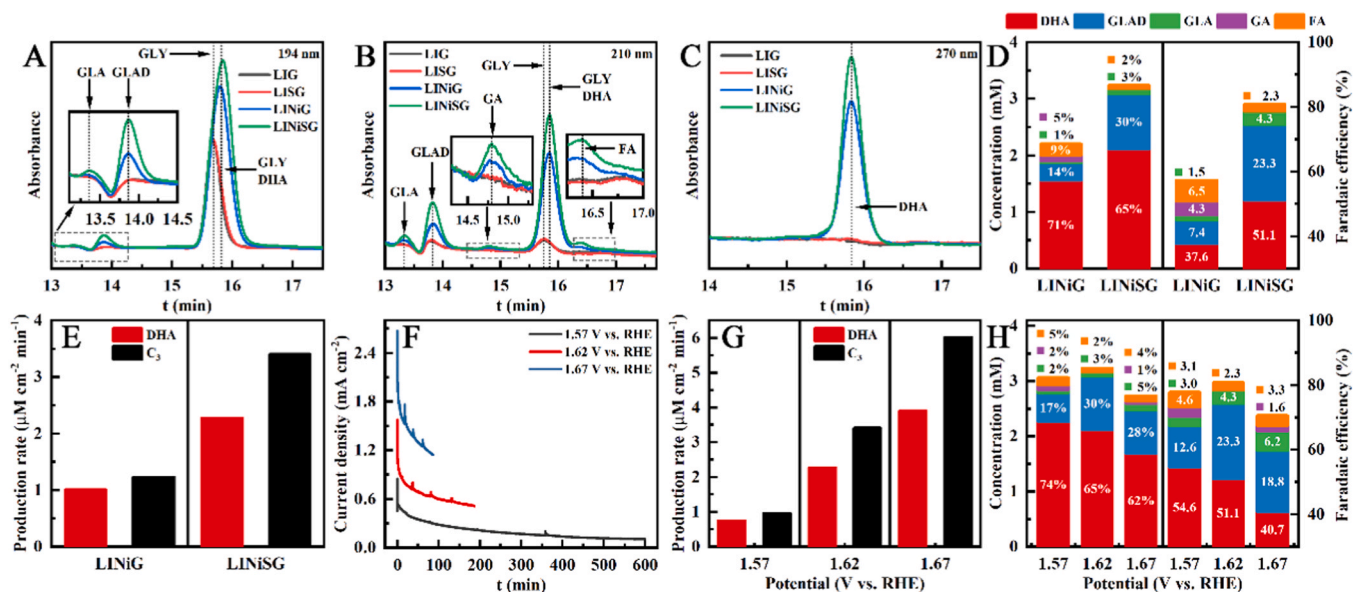


**Fig. 4.** (A–C) HPLC chromatogram of EGOR products detected under different wavelength over LIG, LINiG, LISG, and LINiSG electrodes at 1.62 V<sub>RHE</sub>; (D) Product distribution (left) and corresponding FEs (right) of LINiG and LINiSG electrodes; The percentages in left part indicate the relative selectivity for each product; (E) Production rates of DHA and C<sub>3</sub> chemicals over LINiG and LINiSG electrodes; (F) Chronoamperometry curves and (G) production rates of DHA and C<sub>3</sub> chemicals over LINiSG electrode at 1.57, 1.62, and 1.67 V<sub>RHE</sub>; (H) Product distribution and FEs of LINiSG electrode at different potentials. All experiments were carried out in 0.75 M borate buffer with 100 mM GLY after passing 36 C.

36 C. The LINiSG electrode shows the highest  $S_{C_3}$  (98.0 %) and  $FE_{C_3}$  (78.8 %) at the applied potential of 1.62 V<sub>RHE</sub> with an excellent  $S_{DHA}$  of 65 % and  $FE_{DHA}$  of 51.1 %. As the applied potential further increased, although the production rate shows a significant increase (Fig. 4G), the  $S_{C_3}$  and  $FE_{C_3}$  clearly decline owing to the further oxidation reaction of C<sub>3</sub> chemicals at high potentials. Therefore, comprehensive considering the production rate, FE, and selectivity of both C<sub>3</sub> and DHA, 1.62 V<sub>RHE</sub> was used in further studies. Fig. 5A and Fig. S12 display the laser power-dependent selectivity and FE of EGOR products over LINiSG electrode fabricated at four different laser powers. As summarized in Fig. 5B, the  $S_{C_3}$  remains nearly unchanged while the  $FE_{C_3}$  shows a significant dependence on the laser power with a minimum  $FE_{C_3}$  accounting for 68.6 % when the laser power decreased from 12 % to 10 %. Upon further decreasing of laser power, the total  $FE_{C_3}$  recovers and experiences a further improvement up to a maximum of 88.4 % at 6 % power, where the  $FE_{total}$  is higher than 90 %. The low FE of LINiSG electrode for C<sub>3</sub> compounds at laser power of 10 % is likely influenced by their changed wettability at different laser power. As shown in Fig. 5D, the LINiSG electrode fabricated at 10 % laser power exhibits the smallest contact angle, indicating a highest hydrophilicity, which exhibits a further increasing trend with the increase or decrease of laser power. Although the increased electrode hydrophobicity resulted in the decreased EGOR activity as indicated by the declined current density (Fig. S12), it may enhance the desorption of these C<sub>3</sub> products from the electrode surface, thus leading to the decreased overoxidation of C<sub>3</sub> products. Under each laser power (Fig. 5A), DHA is still the dominant C<sub>3</sub> product with the highest selectivity of 76 % at 8 %, and, however, its FE reaches the maximum of 63.8 % at 6 % power. Interestingly, an obvious increasing trend of  $S_{GLA}$  and  $FE_{GLA}$  is also noticed with the decrease of laser power and finally reaching an amount of 5 % and 9.1 % (Fig. 5A), respectively. This may be due to the slight increase of Ni content in LINiSG electrode evidenced by the ICP-OES measurements (Fig. 5C), which facilitates the consecutive oxidation of GLYD. In contrast, laser power does not contribute significantly to the production rates of these C<sub>3</sub> chemicals (Fig. S13).

Additionally, the temperature-dependent product distributions on LINiSG electrode were compared in the range from 15 to 55 °C (Fig. 5E and Fig. S14) at a fixed applied potential of 1.62 V<sub>RHE</sub>. Apparently, the

LINiSG electrode at higher temperature exhibits higher EGOR activities than the ones at lower temperatures, as demonstrated by the remarkably enhanced current densities at increased temperature (Fig. S14). However, the high temperatures have more negative effects on the valorization of GLY. It is found that the FE, selectivity, and concentration of both C<sub>3</sub> and DHA significantly decline as the temperature increases (Fig. 5E), suggesting a remarkably enhanced overoxidation process of C<sub>3</sub> chemicals and even their derived C<sub>2</sub>/C<sub>1</sub> products to CO<sub>2</sub> at high temperatures from 35 to 55 °C and thus showing the max C<sub>3</sub> and DHA production rate at 25 °C (Fig. 5F). It has been reported that pH has a great influence on EGOR selectivity of Ni-based electrocatalysts. It is found that the product distribution shows a more pH-dependent profile as compared to that of laser-power and temperature. Fig. 5G and Fig. S15 depicted the pH-dependent variation of the resultant selectivity and FE. As the pH increases from 9 to 12, remarkable decreases of  $S_{DHA}$  and  $FE_{DHA}$  were observed, in which case, however, the selectivity and FE values towards GLAD (C<sub>3</sub>), GLA (C<sub>3</sub>), GA (C<sub>2</sub>), and FA (C<sub>1</sub>) increase significantly. Although the current density of LINiSG electrode exhibits an increasing trend with the increase of pH value (Fig. S15), the production rates of both DHA and C<sub>3</sub> chemicals decline remarkably (Fig. 5H). These results suggest that the proposed LINiSG electrode not only exhibited the dominant primary alcohol oxidation over secondary alcohol oxidation in highly basic solution [6], but also show a promoted C–C cleavage reactions even in the presence of borate, therefore denoting a clearly overoxidation of C<sub>3</sub> and their derived C<sub>2</sub> products to final FA (C<sub>1</sub>) product, which is confirmed by the obvious increase in the  $S_{FA}$  and  $FE_{FA}$  especially at pH = 11 and 12. Moreover, it should be noted that there is only a slight decrease in total product concentration and total FE, suggesting that the investigated pHs (<13) is not sufficient to enhance OER or the overoxidation of FA on LINiSG electrode. Furthermore, the EGOR ability of LINiSG electrode towards GLY at higher concentrations was studied in 0.75 M borate buffer (pH = 9) with 0.1, 0.5, and 1.0 M GLY under the same conditions. As displayed in the Fig. S16, S17, further increasing the GLY concentration leads to a remarkable attenuation in the current density during EGOR. Moreover, both FEs and production rates of DHA declined notably with increase of GLY concentration. These are mainly attributed to the weakened borate coordination effect at higher GLY concentration [56]. It has been



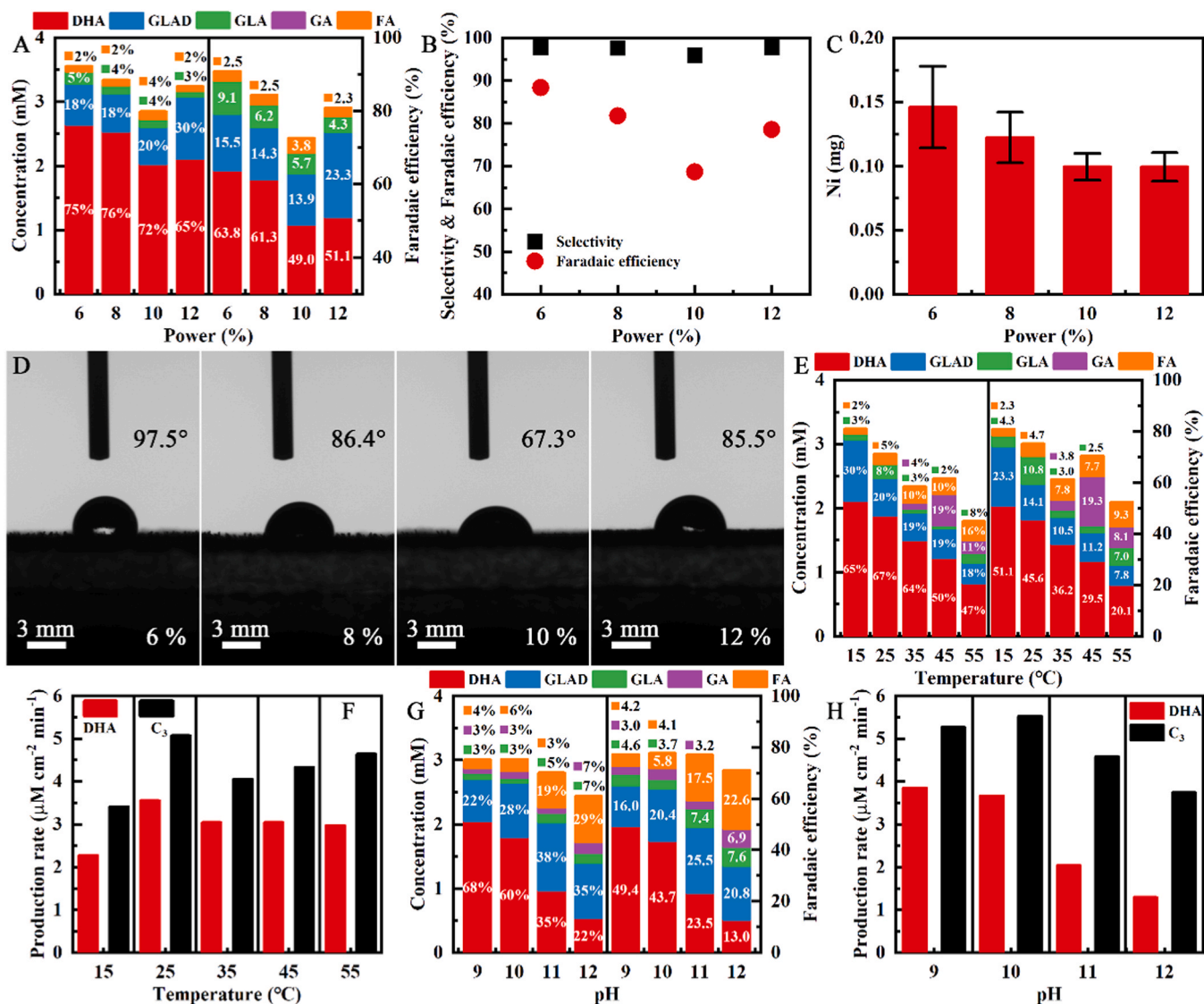


**Fig. 5.** (A) Product distribution (left) and corresponding FEs (right) of LINiSG electrodes fabricated under different laser power; (B)  $\text{S}_{\text{C}_3}/\text{FE}_{\text{C}_3}$ , (C) Ni mass loading, and (D) hydrophilicity of LINiSG electrodes fabricated under different laser power; The full laser power is 40 W. Product distribution (left) and corresponding FEs (right) of LINiSG electrodes at different (E) temperature and (G) pH; Production rates of DHA and C<sub>3</sub> chemicals over LINiSG electrodes at different (F) temperature and (H) pH; All experiments were carried out in 0.75 M borate buffer with 100 mM GLY after passing 36 C at 1.62 V<sub>RHE</sub>.

reported that higher borate/GLY stoichiometric ratio not only favors the oxidation of the secondary hydroxyl group over the primary hydroxyl group, leading to the generation of more DHA, but is also beneficial for protecting DHA from overoxidation. Hence, with the increase in the GLY concentration, there is a decrease in borate/glycerol stoichiometric ratio, thus an obvious increase in GLAD and FA formation is observed, indicating an enhanced C–C bond cleavage of GLY at higher GLY concentration.

For studying how changing the Ni/S doping content in the LINiSG electrode will affect the EGOR product distribution, different LINiSG electrodes were fabricated by changing the Ni concentration as well as the loading volume of Ni-PSU precursor solution. As displayed in Fig. 6A–D and Fig. S18, S19, the current density exhibits a clear trend of enhancing with the increase of both Ni concentration and loading volume, suggesting that the elevated Ni/S doping content can promote the EGOR activity of LINiSG electrode. With the increase of Ni concentration (from 0.1 M to 0.3 M, 10  $\mu\text{L}$ ), no obvious variation tendency of production distribution was observed (Fig. 6A). However, both  $\text{S}_{\text{DHA}}$  and  $\text{FE}_{\text{DHA}}$  attenuates marginally from 64 % and 52.6–60 % and 50.1 %, respectively, when the loading volume of Ni-PSU precursor solution

further changed from 10  $\mu\text{L}$  to 30  $\mu\text{L}$  at 0.3 M (Fig. 6C). As opposed to DHA, the selectivity and FE of GLAD and GLA show less sensitive to the variance of loading volume (Fig. 6C), suggesting that the increase of loading volume contribute more significantly to the overoxidation of DHA. Evidently, the remarkable increase in production rate of C<sub>3</sub> and DHA (Fig. 6B,D) with the increase of both Ni concentration and loading volume denotes a positive effect on increasing the accessibility of active sites and thus enhances EGOR, which increases both the electrocatalytic activity and production rate. To further investigated whether the sulfur content in precursor polymer could influence the EGOR performance of LINiSG electrode, other commercial polysulfone-class polymers, such as polyethersulfone (PES) and polyphenylsulfone (PPSU), were employed to fabricate LINiSG electrodes under the same conditions as described in the experimental section. The sulfur content in PSU, PPSU, and PES is 3.2 %, 3.4 %, and 6.3 % [57], respectively. As displayed in Fig. S20, S21, with the increase of sulfur content from 3.2 % (PSU) to 6.3 % (PES), the  $\text{S}_{\text{DHA}}$  increases slightly from 59 % to 63 % while the  $\text{S}_{\text{GLAD}}$  decreases from 28 % to 24 %. Similar trend was observed in the FE of DHA and GLAD. However, the  $\text{FE}_{\text{C}_3}$  as well as the production rate of both DHA and C<sub>3</sub> chemicals exhibit no obvious dependence on the sulfur content of

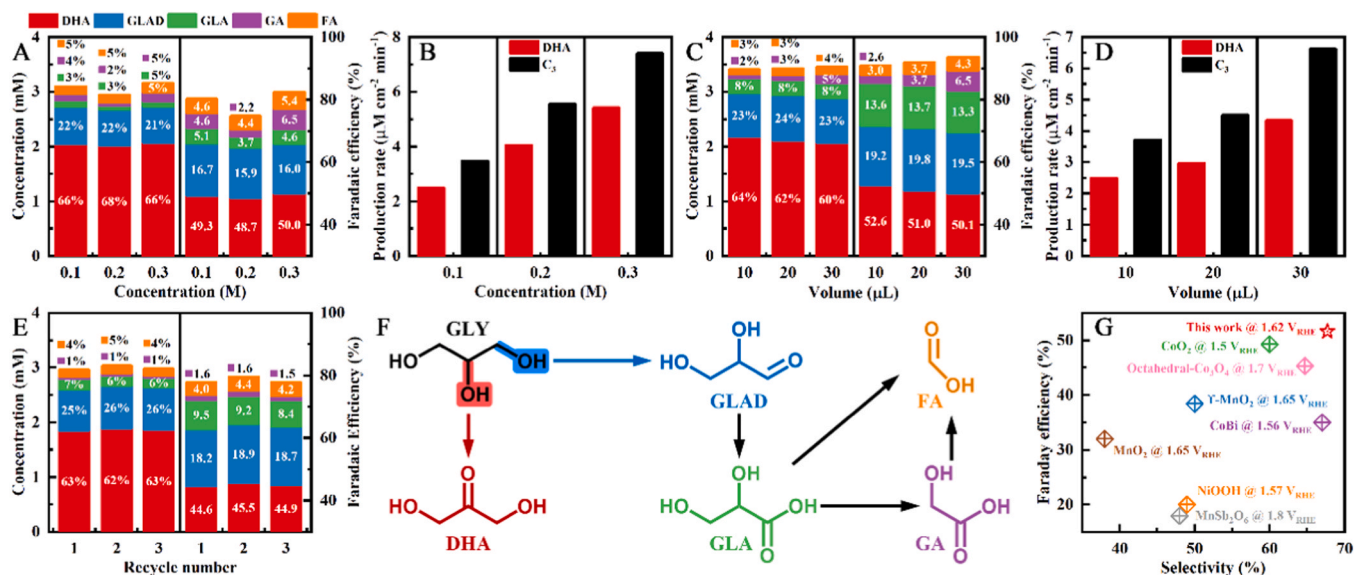


**Fig. 6.** (A,C) Product distribution (left)/FEs (right) and (B,D) DHA and C<sub>3</sub> production rates of LINiSG electrodes fabricated with (A,B) different Ni concentration or (C,D) different loading volume of Ni-PSU precursor solution; The percentages in left part of (A,C) indicate the relative selectivity for each product; (E) Product distribution and FE of LINiSG electrode for three consecutive EGOR cycles; All experiments were carried out in 0.75 M borate buffer with 100 mM GLY after passing 36 C. (F) Schematic illustration of the possible reaction pathway for EGOR on LINiSG electrode; (G) Comparison of the EGOR performance of the LINiSG electrode with other electrocatalysts reported in the literature under similar conditions.

precursor polymers.

The electrocatalytic GOR stability of the LINiSG electrode was then evaluated by successively repeating the chronoamperometric electrolysis experiments. The post-run electrolyte was replaced by a fresh electrolyte after each cycle. The S<sub>C3</sub> and FE<sub>C3</sub> of LINiSG electrode can remain at a constant level (about 95 % and 72 %, respectively) with no significant changes after three consecutive EGOR cycles (Fig. 6E), demonstrating the excellent stability. After the cycle stability test, the SEM images, XPS and Raman spectra of the used LINiSG electrode were characterized. Fig. S22A,B depicts that post-EGOR morphology of LINiSG electrode mostly maintains the 3D hierarchically porous structure of original LIG skeleton, which is also evidenced by the Raman spectra in Fig. S23. However, small nanoparticles/nanoclusters have formed on the edge portions of the multilayered LIG nanosheets and the surface of which seems to become more roughness, possibly due to its inevitable surface oxidation-induced composition evolution during the CV activation process. As expected, the post-EGOR morphology of LINiSG electrode is similar to that of CV-activated LINiSG electrode (Fig. S22C,D). The oxidation-induced surface composition evolution was further verified by XPS spectra. As shown in Fig. S24, the high-resolution Ni 2p XPS spectra of both CV-activated LINiSG electrode and post-EGOR LINiSG electrode is obviously different from the as-prepared one. The peaks corresponding to metallic Ni species (at around 854 eV) significant decreased after CV activation, accompanied with the decrease of the satellite peaks at around 861 eV and 871 eV belonging to metallic Ni<sup>0</sup>, indicating the metallic Ni species is oxidized to higher oxidation states after CV activation, which is beneficial for high EGOR activity. In contrast, the post-EGOR Ni 2p XPS profile of LINiSG electrode after cycle stability test were almost identical with the CV-activated one before EGOR. These results suggest the good durability of LINiSG electrode in EGOR process. It is also interesting to assess the long-term storage stability of LINiSG electrode. LINiSG electrode even exhibited better electrocatalytic GOR performance after two months than freshly prepared one (Fig. S25).

Clearly, DHA and GLAD are the dominant C<sub>3</sub> products of EGOR in this work, implying that the EGOR on LINiSG electrode mainly involves C–H bond breaking through either primary or secondary alcohol oxidation of GLY. Given the detected products, a possible EGOR

oxidation pathway [27] over LINiSG electrode in borate buffer is shown in Fig. 6F. Under mild basic condition (here, pH = 9), the isomerization of DHA to GLAD is inhibited [58], thus the formed GLYD were mainly due to the primary alcohol oxidation of GLY. The obtained DHA is more resistant to further oxidation in near neutral borate electrolyte solution [58] (Fig. S26) and thus could be accumulated to a higher concentration in electrolyte solution as a major organic product. Therefore, the detected GLA is mainly due to the further oxidation of aldehyde group in GLYD. The production of GA and eventually FA is possibly come from the subsequent C–C bond cleavage of GLA. It is instructive to note that, to the best of our understanding, the remarkable S<sub>DHA</sub> (average 67.7 %), FE<sub>DHA</sub> (average 51.6 %), and DHA production rate (average 3.3  $\mu\text{M cm}^{-2} \text{min}^{-1}$ ) obtained in this work is among the highest reported values so far for nonnoble-metal-based electrocatalysts under similar conditions, as displayed in Fig. 6G and Table S1 [6,21,56,59–62].

#### 4. Conclusion

In summary, a self-supported and binder-free monolithic LINiSG electrode with well dispersed Ni-based electrocatalysts in the hierarchical macroporous and hydrophilic structure was successfully prepared by an in-situ laser-induced straightforward solid phase transition procedure under ambient conditions, which achieved high-selective electrocatalytic oxidation of GLY to valuable DHA, GLYD, and GLA in near-neutral conditions with good activity and reasonable stability. The method demonstrated here is more advantageous than the conventional process as it starts with the pre-forming conductive LIG on the flexible PI films, which avoids the use of other expensive current collectors, and is applicable to roll-to-roll manufacturing processes towards large-scale production. Compared with LINiG electrode, the co-carbonization of PSU and Ni precursor is the key to the enhanced EGOR activity and stability, which not only promotes the electrochemical surface area and Ni loading of LINiSG electrode but also leads to the in situ and synchronous formation of S-doped LIG and NiS, as evidenced by physical characterizations. As the main product, the average selectivity for DHA production can reach 67.7 % with an average FE of 51.6 % and production rate of 3.3  $\mu\text{M cm}^{-2} \text{min}^{-1}$ , which outperforms most of the reported EGOR electrode operated in near-neutral conditions. To the best

of our knowledge, this is the first report on the application of self-supported and binder-free monolithic LIG electrode in high-selective EGOR. In view of the advantages and unique properties of LIG, there should be a big room to improve and further exploit LIG electrodes for EGOR, for example, in terms of doping with a co-electrocatalyst as well as changing the morphological and configurational properties of LIG electrode. Therefore, this work will shed light on the application of LIG electrode for electrocatalytic valorization of biomass to value-added C3 products via electrode surface engineering.

### CRedit authorship contribution statement

**Xinzhi Sun:** Supervision, Funding acquisition. **Feng Li:** Writing – review & editing, Funding acquisition. **Xiaojuan Liu:** Visualization. **Lei Ge:** Writing – original draft, Visualization, Funding acquisition. **Zhi-liang Feng:** Visualization, Formal analysis, Data curation. **Zekun Geng:** Software, Data curation. **Shuzhen Pan:** Software, Investigation. **Yaru Yin:** Visualization.

### Declaration of Competing Interest

The authors declare that they have no known competing financial interests or personal relationships that could have appeared to influence the work reported in this paper.

### Data availability

Data will be made available on request.

### Acknowledgements

This work was financially supported by the National Natural Science Foundation of China (22076090, 22274086), the Shandong Provincial Natural Science Foundation (ZR2021MB012, ZR2022ME146), Natural Science Foundation of Qingdao (No. 23-2-1-203-zyyd-jch), the Shandong Province Higher Educational Program for Young Innovation Talents, and the Special Foundation for Taishan Scholar of Shandong Province.

### Appendix A. Supporting information

Supplementary data associated with this article can be found in the online version at [doi:10.1016/j.apcatb.2024.124101](https://doi.org/10.1016/j.apcatb.2024.124101).

### References

- [1] C.O. Tuck, E. Pérez, I.T. Horváth, R.A. Sheldon, M. Poliakoff, Valorization of biomass: deriving more value from waste, *Science* 337 (2012) 695–699.
- [2] P. Sudarsanam, R. Zhong, S. Van den Bosch, S.M. Coman, V.I. Parvulescu, B.F. Sels, Functionalised heterogeneous catalysts for sustainable biomass valorisation, *Chem. Soc. Rev.* 47 (2018) 8349–8402.
- [3] G. Dodekatos, S. Schünemann, H. Tüysüz, Recent advances in thermo-, photo-, and electrocatalytic glycerol oxidation, *ACS Catal.* 8 (2018) 6301–6333.
- [4] Y. Yan, H. Zhou, S.-M. Xu, J. Yang, P. Hao, X. Cai, Y. Ren, M. Xu, X. Kong, M. Shao, Z. Li, H. Duan, Electrocatalytic upcycling of biomass and plastic wastes to biodegradable polymer monomers and hydrogen fuel at high current densities, *J. Am. Chem. Soc.* 145 (2023) 6144–6155.
- [5] J. Wu, X. Liu, Y. Hao, S. Wang, R. Wang, W. Du, S. Cha, X.-Y. Ma, X. Yang, M. Gong, Ligand hybridization for electro-reforming waste glycerol into isolable oxalate and hydrogen, *Angew. Chem. Int. Ed.* 62 (2023) e202216083.
- [6] M.K. Goetz, M.T. Bender, K.-S. Choi, Predictive control of selective secondary alcohol oxidation of glycerol on NiOOH, *Nat. Commun.* 13 (2022) 5848.
- [7] X. Mo, X. Gao, A.V. Gillado, H.-Y. Chen, Y. Chen, Z. Guo, H.-L. Wu, E.C.M. Tse, Direct 3D printing of binder-free bimetallic nanomaterials as integrated electrodes for glycerol oxidation with high selectivity for valuable C3 products, *ACS Nano* 16 (2022) 12202–12213.
- [8] Z. Wang, Q. Hong, B. Miao, T. Wang, Y. Ding, P. Jin, P. Chen, Y. Chen, Organic interfacial engineering of gold nanowires for selective glycerol electrooxidation, *Chin. Chem. Lett.* (2023) 108458.
- [9] J. Wu, J. Li, Y. Li, X.-Y. Ma, W.-Y. Zhang, Y. Hao, W.-B. Cai, Z.-P. Liu, M. Gong, Steering the glycerol electro-reforming selectivity via cation–intermediate interactions, *Angew. Chem. Int. Ed.* 61 (2022) e202113362.
- [10] Y. Xie, L. Sun, X. Pan, Z. Zhou, Y. Zheng, X. Yang, G. Zhao, Carbon paper supported gold nanoflowers for tunable glycerol electrooxidation boosting efficient hydrogen evolution, *Carbon* 203 (2023) 88–96.
- [11] Y. Li, X. Wei, S. Han, L. Chen, J. Shi, MnO<sub>2</sub> electrocatalysts coordinating alcohol oxidation for ultra-durable hydrogen and chemical productions in acidic solutions, *Angew. Chem. Int. Ed.* 60 (2021) 21464–21472.
- [12] G. Wang, J. Chen, K. Li, J. Huang, Y. Huang, Y. Liu, X. Hu, B. Zhao, L. Yi, T. W. Jones, Z. Wen, Cost-effective and durable electrocatalysts for Co-electrolysis of CO<sub>2</sub> conversion and glycerol upgrading, *Nano Energy* 92 (2022) 106751.
- [13] S. Li, P. Ma, C. Gao, L. Liu, X. Wang, M. Shakouri, R. Chernikov, K. Wang, D. Liu, R. Ma, J. Wang, Reconstruction-induced NiCu-based catalysts towards paired electrochemical refining, *Energy Environ. Sci.* 15 (2022) 3004–3014.
- [14] H. Sheng, A.N. Jenes, R.D. Ross, H. Hofstetter, K. Lee, J.R. Schmidt, S. Jin, Linear paired electrochemical valorization of glycerol enabled by the electro-Fenton process using a stable NiSe<sub>2</sub> cathode, *Nat. Catal.* 5 (2022) 716–725.
- [15] L. Zeng, Y. Chen, M. Sun, Q. Huang, K. Sun, J. Ma, J. Li, H. Tan, M. Li, Y. Pan, Y. Liu, M. Luo, B. Huang, S. Guo, Cooperative Rh-O<sub>5</sub>/Ni(Fe) site for efficient biomass upgrading coupled with H<sub>2</sub> production, *J. Am. Chem. Soc.* 145 (2023) 17577–17587.
- [16] K. Yin, Y. Chao, F. Lv, L. Tao, W. Zhang, S. Lu, M. Li, Q. Zhang, L. Gu, H. Li, S. Guo, One Nanometer PtIr nanowires as high-efficiency bifunctional catalysts for electrosynthesis of ethanol into high value-added multicarbon compound coupled with hydrogen production, *J. Am. Chem. Soc.* 143 (2021) 10822–10827.
- [17] H. Wang, L. Jiao, L. Zheng, Q. Fang, Y. Qin, X. Luo, X. Wei, L. Hu, W. Gu, J. Wen, C. Zhu, PdBi single-atom alloy aerogels for efficient ethanol oxidation, *Adv. Funct. Mater.* 31 (2021) 2103465.
- [18] H. Wang, H. Zheng, L. Ling, Q. Fang, L. Jiao, L. Zheng, Y. Qin, Z. Luo, W. Gu, W. Song, C. Zhu, Pd metallene aerogels with single-atom w doping for selective ethanol oxidation, *ACS Nano* 16 (2022) 21266–21274.
- [19] L.S. Oh, M. Park, Y.S. Park, Y. Kim, W. Yoon, J. Hwang, E. Lim, J.H. Park, S. M. Choi, M.H. Seo, W.B. Kim, H.J. Kim, How to change the reaction chemistry on nonprecious metal oxide nanostructure materials for electrocatalytic oxidation of biomass-derived glycerol to renewable chemicals, *Adv. Mater.* 35 (2023) 2203285.
- [20] H. Wan, C. Dai, L. Jin, S. Luo, F. Meng, G. Chen, Y. Duan, C. Liu, Q. Xu, J. Lu, Z. J. Xu, Electro-oxidation of glycerol to high-value-added C1–C3 products by iron-substituted spinel zinc cobalt oxides, *ACS Appl. Mater. Interfaces* 14 (2022) 14293–14301.
- [21] T.-G. Vo, P.-Y. Ho, C.-Y. Chiang, Operando mechanistic studies of selective oxidation of glycerol to dihydroxyacetone over amorphous cobalt oxide, *Appl. Catal. B* 300 (2022) 120723.
- [22] M. Sun, Y. Wang, C. Sun, Y. Qi, J. Cheng, Y. Song, L. Zhang, Nitrogen-doped Co<sub>3</sub>O<sub>4</sub> nanowires enable high-efficiency electrochemical oxidation of 5-hydroxymethylfurfural, *Chin. Chem. Lett.* 33 (2022) 385–389.
- [23] J. Du, Y. Qin, T. Dou, J. Ge, Y. Wang, X. Zhao, F. Zhang, X. Lei, Copper nanoparticles dotted on copper sulfide nanosheets for selective electrocatalytic oxidation of glycerol to formate, *ACS Appl. Nano Mater.* 5 (2022) 10174–10182.
- [24] Y. Xu, T. Liu, K. Shi, H. Yu, K. Deng, X. Wang, Z. Wang, L. Wang, H. Wang, Ru-doping induced lattice strain in hetero-phase Ni<sub>2</sub>P–Ni<sub>12</sub>P<sub>5</sub> arrays enables simultaneous efficient energy-saving hydrogen generation and formate electrosynthesis, *J. Mater. Chem. A* 10 (2022) 20365–20374.
- [25] Z. He, J. Hwang, Z. Gong, M. Zhou, N. Zhang, X. Kang, J.W. Han, Y. Chen, Promoting biomass electrooxidation via modulating proton and oxygen anion deintercalation in hydroxide, *Nat. Commun.* 13 (2022) 3777.
- [26] X. Huang, Y. Guo, Y. Zou, J. Jiang, Electrochemical oxidation of glycerol to hydroxypyruvic acid on cobalt (oxy)hydroxide by high-valent cobalt redox centers, *Appl. Catal. B* 309 (2022) 121247.
- [27] L. Fan, Y. Ji, G. Wang, J. Chen, K. Chen, X. Liu, Z. Wen, High entropy alloy electrocatalytic electrode toward alkaline glycerol valorization coupling with acidic hydrogen production, *J. Am. Chem. Soc.* 144 (2022) 7224–7235.
- [28] X. Han, H. Sheng, C. Yu, T.W. Walker, G.W. Huber, J. Qiu, S. Jin, Electrocatalytic oxidation of glycerol to formic acid by CuCo<sub>2</sub>O<sub>4</sub> spinel oxide nanostructure catalysts, *ACS Catal.* 10 (2020) 6741–6752.
- [29] Y. Li, X. Wei, L. Chen, J. Shi, M. He, Nickel-molybdenum nitride nanoplate electrocatalysts for concurrent electrolytic hydrogen and formate productions, *Nat. Commun.* 10 (2019) 5335.
- [30] Y. Zhang, Z. Xue, X. Zhao, B. Zhang, T. Mu, Controllable and facile preparation of Co<sub>9</sub>S<sub>8</sub>–Ni<sub>3</sub>S<sub>2</sub> heterostructures embedded with N,S,O-tri-doped carbon for electrocatalytic oxidation of 5-hydroxymethylfurfural, *Green. Chem.* 24 (2022) 1721–1731.
- [31] Y. Xin, F. Wang, L. Chen, Y. Li, K. Shen, Superior bifunctional cobalt/nitrogen-codoped carbon nanosheet arrays on copper foam enable stable energy-saving hydrogen production accompanied with glucose upgrading, *Green. Chem.* 24 (2022) 6544–6555.
- [32] D.M. Morales, D. Jambrec, M.A. Kazakova, M. Braun, N. Sikdar, A. Koul, A.C. Brix, S. Seisel, C. Andronescu, W. Schuhmann, Electrocatalytic conversion of glycerol to oxalate on ni oxide nanoparticles-modified oxidized multiwalled carbon nanotubes, *ACS Catal.* 12 (2022) 982–992.
- [33] W. Li, C. Wang, X. Lu, Integrated transition metal and compounds with carbon nanomaterials for electrochemical water splitting, *J. Mater. Chem. A* 9 (2021) 3786–3827.
- [34] H. Zou, B. He, P. Kuang, J. Yu, K. Fan, NixSy nanowalls/nitrogen-doped graphene foam is an efficient trifunctional catalyst for unassisted artificial photosynthesis, *Adv. Funct. Mater.* 28 (2018) 1706917.
- [35] S. Huang, Y. Meng, S. He, A. Goswami, Q. Wu, J. Li, S. Tong, T. Asefa, M. Wu, N-, O-, and S-tridoped carbon-encapsulated co<sub>9</sub>s<sub>8</sub> nanomaterials: efficient bifunctional electrocatalysts for overall water splitting, *Adv. Funct. Mater.* 27 (2017) 1606585.



- [36] N. Logeshwaran, I.R. Panneerselvam, S. Ramakrishnan, R.S. Kumar, A.R. Kim, Y. Wang, D.J. Yoo, Quasi-hexagonal platinum nanodendrites decorated over CoS<sub>2</sub>-N-doped reduced graphene oxide for electro-oxidation of C1-, C2-, and C3-type alcohols, *Adv. Sci.* 9 (2022) 2105344.
- [37] Y. Xu, M. Liu, S. Wang, K. Ren, M. Wang, Z. Wang, X. Li, L. Wang, H. Wang, Integrating electrocatalytic hydrogen generation with selective oxidation of glycerol to formate over bifunctional nitrogen-doped carbon coated nickel-molybdenum-nitrogen nanowire arrays, *Appl. Catal. B* 298 (2021) 120493.
- [38] D. Lee, Y. Kim, Y. Kwon, J. Lee, T.-W. Kim, Y. Noh, W.B. Kim, M.H. Seo, K. Kim, H. J. Kim, Boosting the electrocatalytic glycerol oxidation performance with highly-dispersed Pt nanoclusters loaded on 3D graphene-like microporous carbon, *Appl. Catal. B* 245 (2019) 555–568.
- [39] M.S.E. Houache, R. Safari, U.O. Nwabara, T. Rafaideen, G.A. Botton, P.J.A. Kenis, S. Baranton, C. Coutanceau, E.A. Baranova, Selective electrooxidation of glycerol to formic acid over carbon supported Ni1-xMx (M = Bi, Pd, and Au) nanocatalysts and coelectrolysis of CO<sub>2</sub>, *ACS Appl. Energy Mater.* 3 (2020) 8725–8738.
- [40] T.-G. Vo, G.-S. Tran, C.-L. Chiang, Y.-G. Lin, H.-E. Chang, H.-H. Kuo, C.-Y. Chiang, Y.-J. Hsu, Au@NiSx Yolk@shell nanostructures as dual-functional electrocatalysts for concomitant production of value-added tartronic acid and hydrogen fuel, *Adv. Funct. Mater.* 33 (2023) 2209386.
- [41] G. Ma, N. Yang, G. Zhou, X. Wang, The electrochemical reforming of glycerol at Pd nanocrystals modified ultrathin NiO nanoplates hybrids: An efficient system for glyceraldehyde and hydrogen coproduction, *Nano Res* 15 (2022) 1934–1941.
- [42] J. Lin, Z. Peng, Y. Liu, F. Ruiz-Zepeda, R. Ye, E.L.G. Samuel, M.J. Yacaman, B. I. Yakobson, J.M. Tour, Laser-induced porous graphene films from commercial polymers, *Nat. Commun.* 5 (2014) 5714.
- [43] R. Ye, D.K. James, J.M. Tour, Laser-Induced Graphene, *Acc. Chem. Res.* 51 (2018) 1609–1620.
- [44] A.C. Bressi, A. Dallinger, Y. Steksova, F. Greco, Bioderived laser-induced graphene for sensors and supercapacitors, *ACS Appl. Mater. Interfaces* 15 (2023) 35788–35814.
- [45] Q. Zhang, F. Zhang, X. Liu, Z. Yue, X. Chen, Z. Wan, Doping of laser-induced graphene and its applications, *Adv. Mater. Technol.* 8 (2023) 2300244.
- [46] R. Ye, D.K. James, J.M. Tour, Laser-Induced Graphene: from Discovery to Translation, *Adv. Mater.* 31 (2019) 1803621.
- [47] Y. Wang, Y. Zhao, X. Li, L. Jiang, L. Qu, Laser-based growth and treatment of graphene for advanced photo- and electro-related device applications, *Adv. Funct. Mater.* 32 (2022) 2203164.
- [48] L. Ge, Q. Hong, H. Li, C. Liu, F. Li, Direct-laser-writing of metal sulfide-graphene nanocomposite photoelectrode toward sensitive photoelectrochemical sensing, *Adv. Funct. Mater.* 29 (2019) 1904000.
- [49] H. Liu, Z. Sun, Y. Chen, W. Zhang, X. Chen, C.-P. Wong, Laser processing of flexible in-plane micro-supercapacitors: progresses in advanced manufacturing of nanostructured electrodes, *ACS Nano* 16 (2022) 10088–10129.
- [50] L. Huang, L. Cheng, T. Ma, J.-J. Zhang, H. Wu, J. Su, Y. Song, H. Zhu, Q. Liu, M. Zhu, Z. Zeng, Q. He, M.-K. Tse, D.-T. Yang, B.I. Yakobson, B.Z. Tang, Y. Ren, R. Ye, Direct Synthesis of Ammonia from Nitrate on Amorphous Graphene with near 100 % Efficiency, *Adv. Mater.* 35 (2023) 2211856.
- [51] W. Li, J.-W. Zhao, C. Yan, B. Dong, Y. Zhang, W. Li, J. Zai, G.-R. Li, X. Qian, Asymmetric activation of the nitro group over a Ag/graphene heterointerface to boost highly selective electrocatalytic reduction of nitrobenzene, *ACS Appl. Mater. Interfaces* 14 (2022) 25478–25489.
- [52] G. Yang, J. Liu, M. Zhou, J. Bai, X. Bo, Fast and facile room-temperature synthesis of MOF-derived Co nanoparticle/nitrogen-doped porous graphene in air atmosphere for overall water splitting, *ACS Sustain. Chem. Eng.* 8 (2020) 11947–11955.
- [53] M. Ren, H. Zheng, J. Lei, J. Zhang, X. Wang, B.I. Yakobson, Y. Yao, J.M. Tour, CO<sub>2</sub> to formic acid using Cu-Sn on laser-induced graphene, *ACS Appl. Mater. Interfaces* 12 (2020) 41223–41229.
- [54] X. Du, X. Lei, L. Zhou, Y. Peng, Y. Zeng, H. Yang, D. Li, C. Hu, H. Garcia, Bimetallic Ni and Mo nitride as an efficient catalyst for hydrodeoxygenation of palmitic acid, *ACS Catal.* 12 (2022) 4333–4343.
- [55] H. Li, X. Xia, C. Guo, L. Ge, F. Li, Laser-induced nano-bismuth decorated CdS-graphene hybrid for plasmon-enhanced photoelectrochemical analysis, *Chem. Commun.* 56 (2020) 13784–13787.
- [56] X. Huang, Y. Zou, J. Jiang, Electrochemical oxidation of glycerol to dihydroxyacetone in borate buffer: enhancing activity and selectivity by borate-polyol coordination chemistry, *ACS Sustain. Chem. Eng.* 9 (2021) 14470–14479.
- [57] S.P. Singh, Y. Li, J. Zhang, J.M. Tour, C.J. Arnsch, Sulfur-doped laser-induced porous graphene derived from polysulfone-class polymers and membranes, *ACS Nano* 12 (2018) 289–297.
- [58] C. Liu, M. Hirohara, T. Maekawa, R. Chang, T. Hayashi, C.-Y. Chiang, Selective electro-oxidation of glycerol to dihydroxyacetone by a non-precious electrocatalyst – CuO, *Appl. Catal. B* 265 (2020) 118543.
- [59] M.K. Goetz, E. Usman, K.-S. Choi, Understanding and Suppressing C–C Cleavage during Glycerol Oxidation for C3 Chemical Production, *ACS Catal.* 13 (2023) 15758–15769.
- [60] G.-S. Tran, T.-G. Vo, C.-Y. Chiang, Operando revealing the crystal phase transformation and electrocatalytic activity correlation of MnO<sub>2</sub> toward glycerol electrooxidation, *ACS Appl. Mater. Interfaces* 15 (2023) 22662–22671.
- [61] G.-S. Tran, T.-G. Vo, C.-Y. Chiang, Earth-abundant manganese oxide nanoneedle as highly efficient electrocatalyst for selective glycerol electro-oxidation to dihydroxyacetone, *J. Catal.* 404 (2021) 139–148.
- [62] T.-G. Vo, P.-Y. Tsai, C.-Y. Chiang, Tuning selectivity and activity of the electrochemical glycerol oxidation reaction by manipulating morphology and exposed facet of spinel cobalt oxides, *J. Catal.* 424 (2023) 64–73.